



# Suppressing hydrogen evolution in copper oxides for CO<sub>2</sub> electroreduction by tuning metal oxide supports

Nathan R. Harrison<sup>1</sup> · Aziz Genc<sup>2</sup> · Thomas J. A. Slater<sup>2</sup> · Andrea Folli<sup>1</sup>

Received: 7 February 2025 / Revised: 7 April 2025 / Accepted: 8 April 2025  
© The Author(s) 2025

## Abstract

In this work, a range of supported copper oxides were synthesised via a simple deposition precipitation method, and their catalytic performance for the hydrogen evolution reaction (HER) was analysed, evaluating the influence of the support on catalytic activity. Electrochemical measurements showed that Cu<sub>2</sub>O containing catalysts had superior HER activity compared to CuO containing catalysts, achieving lower HER overpotentials and Tafel slope values. The SnO<sub>2</sub> support showed the largest HER suppression, desirable for use within the CO<sub>2</sub> reduction reaction (CO<sub>2</sub>RR), reducing the activity of the competing reaction, achieving a large HER overpotential value of 0.73 V vs. RHE, along with a small HER exchange current density of 5.93 μA/cm<sup>2</sup>, for Cu<sub>2</sub>O/SnO<sub>2</sub>, shown to be through possessing large HER charge-transfer resistance and small electrochemically active surface areas. The ZnO support was also shown to be adequate at suppressing the HER activity, whilst also achieving the highest electrochemically active surface area for the reduction reactions to proceed on, out of all supported catalysts assessed in this work.

**Keywords** HER · CO<sub>2</sub>RR · Metal oxides · Supported electrocatalysts

## Introduction

Conversion of CO<sub>2</sub> into energy-rich chemicals has the potential to be a viable route to help reduce atmospheric carbon emission (30 billion tonnes of CO<sub>2</sub> are estimated to be globally emitted each year [1]) and to generate carbon-neutral fuels [2]. CO<sub>2</sub> conversion presents numerous challenges stemming from the molecule's intrinsic chemical properties, notably the presence of two strong polar C=O bonds [1]. This structure causes a highly stable molecule, with a C=O bond energy of 805 kJ mol<sup>-1</sup>, significantly stronger than other carbon-based bonds [3]. This results in large energy inputs being required to overcome the thermodynamically uphill nature of the CO<sub>2</sub> reduction reaction (CO<sub>2</sub>RR). Electrocatalytic (EC) CO<sub>2</sub> reduction meets the challenge of large

energy input by converting electrical energy to chemical energy. Electrochemical reduction takes place via redox events at electrode surfaces [1], with the electron source in EC enabling multi-electron processes to take place in the CO<sub>2</sub> reduction reaction (CO<sub>2</sub>RR).

In addition to thermodynamic considerations, the CO<sub>2</sub>RR also experiences extremely sluggish kinetics due to high activation energy barriers [4], resulting in much more negative potentials being required to be applied to the working electrode. Additionally, it is possible to generate a wide range of reduction products, resulting in desired product selectivity being extremely challenging. Kinetic and selectivity issues suggest that choice of catalyst is highly important for this reaction.

Copper has been reported to be the most efficient metal in CO<sub>2</sub> EC conversion through its moderate adsorption energies of reactive intermediates [5]. Along with this, copper is reported as a unique metal for CO<sub>2</sub>RR, as not only is it capable of generating C<sub>1</sub> products, but it is also the only reported metal to generate C<sub>2+</sub> products with sufficient Faradaic efficiencies (FEs) [6] for further use, with Hori et al. [7] reporting copper achieving a total C<sub>2+</sub> FE's of 34.2%, with the next best metal being Ni with a FE of only 0.1%. Along with this, Hori et al. [7] also reported copper to be the only

✉ Andrea Folli  
folli@cardiff.ac.uk

<sup>1</sup> School of Chemistry, Cardiff Catalysis Institute, Net Zero Innovation Institute, Cardiff University, Cardiff CF24 4HF, UK

<sup>2</sup> School of Chemistry, Cardiff Catalysis Institute, Cardiff University, Cardiff CF24 4HF, UK

metal to generate sufficient FE's of methane of 33.3%, along with the C<sub>2+</sub> products, with these experiments being done at a constant current density of 5 mA/cm<sup>2</sup>. This is due to copper ability to facilitate carbon coupling to longer chains through its excellent bonding with reactive intermediates, such as CO [8]. Along with its unique activity for CO<sub>2</sub>RR, copper is an abundant and low-toxicity metal, which has led to substantial amounts of research into copper for CO<sub>2</sub>RR.

However, there are still reported issues with using copper and its derivatives for CO<sub>2</sub>RR, with catalysts reported to achieve low product selectivity, forming a range of products from C<sub>1</sub> and beyond [9, 10]. From an electrochemical perspective, one of the biggest challenges within CO<sub>2</sub>RR is the parasite hydrogen evolution reaction (HER), which is unavoidable in the aqueous electrolytes ordinarily used, with HER dominating at the highly negative potentials required to overcome the energies needed to reduce the stable CO<sub>2</sub> molecule, hence greatly affecting the CO<sub>2</sub>RR FEs. Additionally, copper is only usable in a narrow potential window, with low negative potentials being insufficient to reduce CO<sub>2</sub>, whereas at higher negative potentials the HER dominates [11], resulting in extremely low FEs, unless the HER can be suppressed. HER occurs through two main mechanisms, the simplest being via the reduction of solvated protons ( $2\text{H}^+ + 2\text{e}^- \rightarrow \text{H}_2$ ), most prominent at lower pH. However, the HER also occurs through the reduction of the solvent molecule itself ( $2\text{H}_2\text{O} + 2\text{e}^- \rightarrow \text{H}_2 + 2\text{OH}^-$ ) [13], hence still proceeding at the alkaline pH typically used within CO<sub>2</sub>RR [12]. Although unavoidable in aqueous media, HER efficiency can be reduced through rational catalyst design.

Amongst the most promising strategies adopted to improve CO<sub>2</sub>RR performance whilst suppressing HER, the use of suitable supports for the Cu-based electrocatalysts is a widely adopted approach [14]. Yuan et al. [15] and Lu et al. [16] have reported that a CuO/TiO<sub>2</sub> catalyst system favours the formation of ethanol during CO<sub>2</sub>RR, with Yuan et al. [15] producing ethanol with a FE of 37.5%, whereas Lu et al. [16] showed ethanol FE of 74% with a product yield of 1.6 μmol/cm<sup>2</sup>, when using TiO<sub>2</sub> nanotubes, compared to a maximum ethanol FE of 55% and a maximum yield of 6.4 μmol/cm<sup>2</sup> when using TiO<sub>2</sub> nanofibers. Zhang et al. [17] reported a Cu<sub>2</sub>O/TiO<sub>2</sub> catalyst that favours the production of ethanol, with a fivefold FE increase compared to bare Cu<sub>2</sub>O; nevertheless, the FE loss to HER was 70%. The increased generation of ethanol correlated to the introduction of TiO<sub>2</sub> is reconciled with an increased catalyst oxophilicity caused by the titanium dioxide, therefore strengthening the CO bridge binding. Just like TiO<sub>2</sub>, tin dioxide (SnO<sub>2</sub>) is another metal that can be used to increase the catalyst oxophilicity, with bare SnO<sub>2</sub> generating formate from CO<sub>2</sub> [18]. Li et al. [19] covered Cu NPs with SnO<sub>2</sub>, resulting in a

product selectivity change from formate to CO, with a Faradaic efficiency of 93% at -0.7 V vs. RHE. Zhang et al. [20] also showed this Cu and Sn synergy for CO through a Cu<sub>2</sub>O/SnO<sub>2</sub> core shell catalyst, obtaining a CO Faradaic efficiency greater than 90%. The mechanism of FE enhancement when SnO<sub>2</sub> is used was illustrated by computational studies of Sarfraz et al. [21], demonstrating inhibition of hydride adsorption, increasing CO production at the expenses of HER and formate selectivity.

It has also previously been reported that bare ZnO and metallic zinc are capable of reducing CO<sub>2</sub> to CO [22, 23]. Combined copper and zinc systems are already well studied, and industrially used, for methanol synthesis [24], with the addition of ZnO to Cu increasing the catalyst basicity [25], improving CO<sub>2</sub> adsorption. Azenha et al. [26] synthesised a Cu<sub>2</sub>O/ZnO catalyst, showing production of CO with FE of 65.7% at -1.4 V vs. RHE; although with a large HER FE loss greater than 30%. Graphitic carbon nitride (GCN), containing pyridinic N, has been shown to help generate C<sub>2+</sub> products through C-C coupling via its affinity to the CO reaction intermediate [22]. Jiao et al. [27] conducted computational studies on Cu/GCN and reported that pyridinic nitrogen species in the framework show a strong affinity for CO<sub>2</sub>, activating the molecule for its reduction. Yan and Wu [28] showed this experimentally with a CuO/GCN catalyst, generating a C<sub>2</sub> FE of 64.7% at -1 V vs. RHE, with ethylene being the main C<sub>2</sub> product with 37% FE. However, even with this increased C<sub>2</sub> product generation, there was still a large FE loss through the competing HER of 25%. Rutkowska et al. [29] synthesised a Cu<sub>2</sub>O catalyst decorated in WO<sub>3</sub> nanowires, reporting an increase in current density when the buffer solution was saturated with CO<sub>2</sub>, showing its CO<sub>2</sub>RR activity. Product analysis showed that the Cu<sub>2</sub>O/WO<sub>3</sub> catalyst main product was methanol, with hydrogen being the only detected gaseous product, limiting the methanol FE.

The published work outlined here gives a handful of examples of how pairing copper with an additional support material can help improve FE during electrocatalytic CO<sub>2</sub> reduction. However, due to the different experimental conditions adopted and the variability of the samples, it is difficult to rationalise the actual effect of these supports in suppressing parasitic HER. In this work, we attempt to provide a standardised approach to quantify the effect of support materials in suppressing HER when Cu-based electrocatalysts are used. A series of supported CuO and Cu<sub>2</sub>O electrocatalysts have been synthesised with the same Cu-to-support ratio, and characterised and tested for their HER performance. A comparison with unsupported CuO and Cu<sub>2</sub>O is provided. The aim of this study is to identify which support material provides the best performance to suppress HER when running CO<sub>2</sub>RR.

## Materials and methods

### Electrocatalyst synthesis

Copper chloride dihydrate ( $\text{CuCl}_2 \cdot 2\text{H}_2\text{O}$ ), titanium dioxide anatase ( $\text{TiO}_2$ ), zinc oxide ( $\text{ZnO}$ ), tin oxide ( $\text{SnO}_2$ ), and tungsten oxide ( $\text{WO}_3$ ) were all purchased from Sigma Aldrich. Ascorbic acid ( $\text{C}_6\text{H}_8\text{O}_6$ ) was purchased from Fluorochem. Melamine ( $\text{C}_3\text{H}_6\text{N}_3$ ) and sodium hydroxide ( $\text{NaOH}$ ) were purchased from Thermo Fisher Scientific. All chemicals were analytical grade and used without further purification. Deionised water was used to make up all the solutions.

The bare copper oxide catalysts were synthesised through a metal oxide precipitation method. A  $\text{CuCl}_2 \cdot 2\text{H}_2\text{O}$  solution was first sonicated for 15 min before a sodium hydroxide solution was slowly dropped into the copper solution, under constant stirring, to form  $\text{Cu}(\text{OH})_2$  precipitate. In the case of  $\text{CuO}$ , the solution was then aged for 4 h. For  $\text{Cu}_2\text{O}$ , 3 h through the ageing step, an ascorbic acid solution is slowly added as a reducing agent. The resulting precipitates are filtered, washed, and dried. The copper oxides are then calcined under static air in a tubular furnace, at 200 °C for  $\text{Cu}_2\text{O}$  and 350 °C for  $\text{CuO}$ , for 2 h with a ramp rate of 3°/min.

For the copper oxides supported by another metal oxide, a simple deposition precipitation synthesis method was used. First, the support is suspended in a solution and sonicated for 15 min. Then, a certain amount of  $\text{CuCl}_2 \cdot 2\text{H}_2\text{O}$  is added to the solution to result in a 1:10 copper to support transition metal molar ratio. The solution is then stirred for an hour before slow addition of a sodium hydroxide solution, in the same way as described above. The  $\text{CuO}$  catalysts are then aged for 4 h, whereas for  $\text{Cu}_2\text{O}$ , 3 h through the ageing step, an ascorbic acid solution is slowly added. The resulting precipitates are filtered, washed, and dried. The supported copper oxides are then calcined under static air in a tubular furnace, at 200 °C for  $\text{Cu}_2\text{O}$  and 350 °C for  $\text{CuO}$ , for 2 h with a ramp rate of 3°/min.

The  $\text{CuO/g-C}_3\text{N}_4$  and  $\text{Cu}_2\text{O/g-C}_3\text{N}_4$  catalysts are synthesised in the same way as previously described, but with a prior  $\text{g-C}_3\text{N}_4$  synthesis step. The graphitic carbon nitride (GCN) support was synthesised via a thermal polycondensation reaction from melamine. Roughly 3 g of melamine was placed in a crucible and heated to 550 °C in a static air muffle furnace, at a heating ramp of 5°/min for 5 h.

### Material characterisation

Powder X-ray diffraction (XRD) was carried out to investigate the materials' crystal phases and polymorphs using

a PANalyticalX'pert Pro powder diffractometer, using a  $\text{Cu K}\alpha$  radiation source ( $\lambda = 1.54 \times 10^{-10} \text{ m}$ ), operating at 40 keV and 40 mA. Analysis was done between  $2\theta$  values of 10–80°, with diffraction pattern phases identified using the ICDD database. High-resolution transmission electron microscopy (HRTEM) images were obtained via a JEOL JEM- 2100 electron microscope, employing an accelerating voltage of 200 kV. Particle diameters were manually measured using ImageJ, with the standard deviation of at least 30 measurements reported as the error here.

### Electrochemical measurements

Sodium phosphate monobasic ( $\text{NaH}_2\text{PO}_4$ ), sodium phosphate dibasic ( $\text{Na}_2\text{HPO}_4$ ), and Nafion 117 solution (5% suspended in lower aliphatic alcohols and water) were all purchased from Sigma Aldrich. Isopropanol (IPA) was purchased from Thermo Fisher Scientific. All chemicals were analytical grade and used without further purification. Deionised water was used to make up all the solutions.

For each catalyst, a stable ink was prepared using 8 mg of synthesised powder catalyst, 380  $\mu\text{L}$  IPA, 380  $\mu\text{L}$   $\text{H}_2\text{O}$ , 40  $\mu\text{L}$  Nafion solution, and then sonicated for 20 min before 10  $\mu\text{L}$  of the stable ink were drop cast onto a 0.4-cm diameter glassy carbon rotating disk electrode (RDE) tip and left to dry, resulting in a catalyst loading (on the glassy carbon disk) of 0.1 mg.

All electrochemical tests were performed using a three-electrode undivided electrochemical cell consisting of (i) an Ivium rotating disk electrode (RDE) carrying the coated glassy carbon tip, as described above, and constituting the working electrode (WE); (ii) a 3.0 M  $\text{Ag}/\text{AgCl}$  reference electrode; and (iii) a platinum coil counter electrode, all immersed in a 0.5 M  $\text{Na}_2\text{HPO}_4$  + 0.5 M  $\text{NaH}_2\text{PO}_4$  buffered aqueous electrolyte at a pH of 7.2.

Before any electrochemical measurements, the electrolyte solution was saturated with  $\text{N}_2$  for 20 min. The WE was then pretreated via running 10 cyclic voltammetry (CV) scans at a 500 rpm rotation rate in the  $-0.6$  to  $0.0$  V vs. RHE potential range, with the potential scanned at a rate of 50 mV/s. The HER tests were performed via running linear sweep voltammetry (LSV) anodically in the  $-1.0$  to  $0.0$  V vs. RHE range, at a scan rate of 20 mV/s, at different rotation rates of 500, 1000, 1500, and 2000 rpm, with all current densities reported against the electrodes electrochemically active surface area (ECSA). The double layer capacitance ( $C_{dl}$ ) was derived via running CVs in the non-faradaic potential range of 0.23 to 0.43 V vs. RHE at different scan rates of 10, 20, 30, 40, and 50 mV/s. The  $C_{dl}$  is equal to the gradient of the linear relationship between  $(J_{anodic} - J_{cathodic})/2$ , taken at 0.33 V vs. RHE from a single CV, against scan rate. Electrochemical impedance spectroscopy (EIS) was performed at various

amplitude potentials of 10, 50, 100, and 200 mV (vs. Ag/AgCl), at each catalyst HER onset potential in the frequency region of 100 kHz to 0.1 Hz, whilst the RDE working electrode was rotating at 2000 rpm.

## Results and discussion

### Characterising crystallography and morphology

Figure 1 depicts the XRD patterns of all the synthesised catalysts, with the produced patterns having strong matches to reference patterns present in the ICDD database for the expected synthesised materials. The stronger peak intensities in bare  $\text{Cu}_2\text{O}$  compared to CuO show the more crystalline nature and larger crystallite size of the  $\text{Cu}_2\text{O}$  catalyst. The XRD patterns for all the supported copper oxides strongly match that of the support material. The dominance of the support material peaks is due to the 1:10 molar composition ratio of copper to the support transition metal, resulting in the produced pattern strongly matching that of the support. This is consistent with all the supported catalysts, with only some weak intensity copper oxide peaks observed; this can be seen better in the supporting information (SI Figs. 2 and 3) where all catalyst XRD patterns are compared to references patterns. All XRD patterns for the bare and supported CuO catalysts aligned with the monoclinic phase pattern, with the C2/c space group. Whereas for all the  $\text{Cu}_2\text{O}$  catalysts, all XRD patterns match that of the cubic phase in the Pn-3 m space group.

Transmission electron microscopy (TEM) was conducted to verify crystallinity and morphology of the Cu

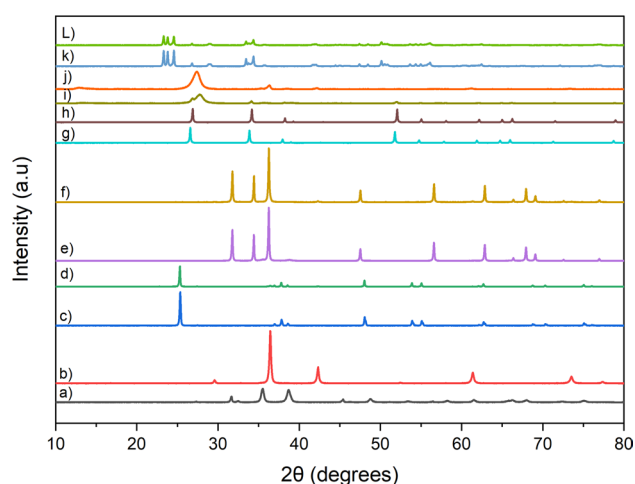


**Fig. 1** XRD patterns of all synthesised catalysts: **a)** CuO, **b)**  $\text{Cu}_2\text{O}$ , **c)** CuO/ $\text{TiO}_2$ , **d)**  $\text{Cu}_2\text{O}/\text{TiO}_2$ , **e)** CuO/ $\text{ZnO}$ , **f)**  $\text{Cu}_2\text{O}/\text{ZnO}$ , **g)** CuO/ $\text{SnO}_2$ , **h)**  $\text{Cu}_2\text{O}/\text{SnO}_2$ , **i)** CuO/ $\text{g-C}_3\text{N}_4$ , **j)**  $\text{Cu}_2\text{O}/\text{g-C}_3\text{N}_4$ , **k)** CuO/ $\text{WO}_3$ , **l)**  $\text{Cu}_2\text{O}/\text{WO}_3$

oxide electrocatalysts. A representative CuO HRTEM image (Fig. 2(a)) shows that CuO is present as nanoparticles with an average diameter of  $30 \pm 6$  nm. Analysis of Fourier transforms of the CuO HRTEM images shows that the monoclinic CuO phase is present, visualised in Fig. 2(a) along its [101] zonal axis (additional orientation in SI Fig. 4). The  $\text{Cu}_2\text{O}$  nanoparticles can be seen in Fig. 2b, with a representative Fourier transform of an individual nanoparticle revealing the cubic  $\text{Cu}_2\text{O}$  phase being present, being visualised through its [001] zone axis. Sizes of the  $\text{Cu}_2\text{O}$  nanoparticles are larger and have a higher size variation, between 30 and 200 nm, compared to the CuO nanoparticles. These HRTEM results are in agreement with the presented XRD data, with the produced CuO XRD pattern matching the monoclinic phase, in the C2/c space group. The  $\text{Cu}_2\text{O}$  XRD pattern is also in agreement with the  $\text{Cu}_2\text{O}$  HRTEM, with the cubic phase being present, in the Pn-3 m space group. The HRTEM images also showed some nanoparticles having partial  $\text{Cu}_2\text{O}$  oxidation to CuO in a core shell like morphology; this can be seen better in the HRTEM images provided in the supporting information (SI Fig. 5), with this partial oxidation being due to the unstable  $\text{Cu}_2\text{O}$  catalyst being stored in aerobic conditions. Examples of deposited CuO and  $\text{Cu}_2\text{O}$  are here presented for the ZnO and  $\text{SnO}_2$  cases. The CuO/ $\text{ZnO}$  catalysts are composed of large ZnO nanoparticles decorated with smaller CuO nanoparticles, as seen in Fig. 2c. The larger ZnO nanoparticles are present as hexagonal ZnO phases, with the {002}, {111}, and {011} planes observed. The smaller CuO nanoparticles on top of ZnO are shown to be the same monoclinic CuO phase as before, visualised along the [110] and [011] zone axes (the latter can be seen in SI Fig. 6), matching the phase observed in the XRD data. The  $\text{Cu}_2\text{O}/\text{ZnO}$  catalyst shows the same hexagonal ZnO phases as before, which is expected using the same ZnO for the two different deposition precipitation synthesis methods. Along with these ZnO phases, the HRTEM images show nanoparticles of the cubic  $\text{Cu}_2\text{O}$  phase, visualised along their [001] and [010] zone axes, the same as observed for the bare  $\text{Cu}_2\text{O}$  and in the XRD pattern of the ZnO supported  $\text{Cu}_2\text{O}$ . Figure 2e shows the HRTEM images of the CuO/ $\text{SnO}_2$  catalyst, with the CuO and  $\text{SnO}_2$  nanoparticles having similar size and morphology. Almost all the  $\text{SnO}_2$  nanoparticles were shown to be in the rutile phase, visualised through the [001] and [111] zone axes, with the CuO nanoparticles being present again in the monoclinic CuO phase, as previously seen for the bare CuO and CuO/ $\text{ZnO}$  catalyst in both the TEM and XRD data. The HRTEM images for all remaining catalysts presented in this work, along with further TEM images of the catalysts described above, can be found in the supporting information, with all catalysts following the same pattern of CuO nanoparticles found in the monoclinic phase and  $\text{Cu}_2\text{O}$  in the cubic phase, supporting the previously presented XRD data.

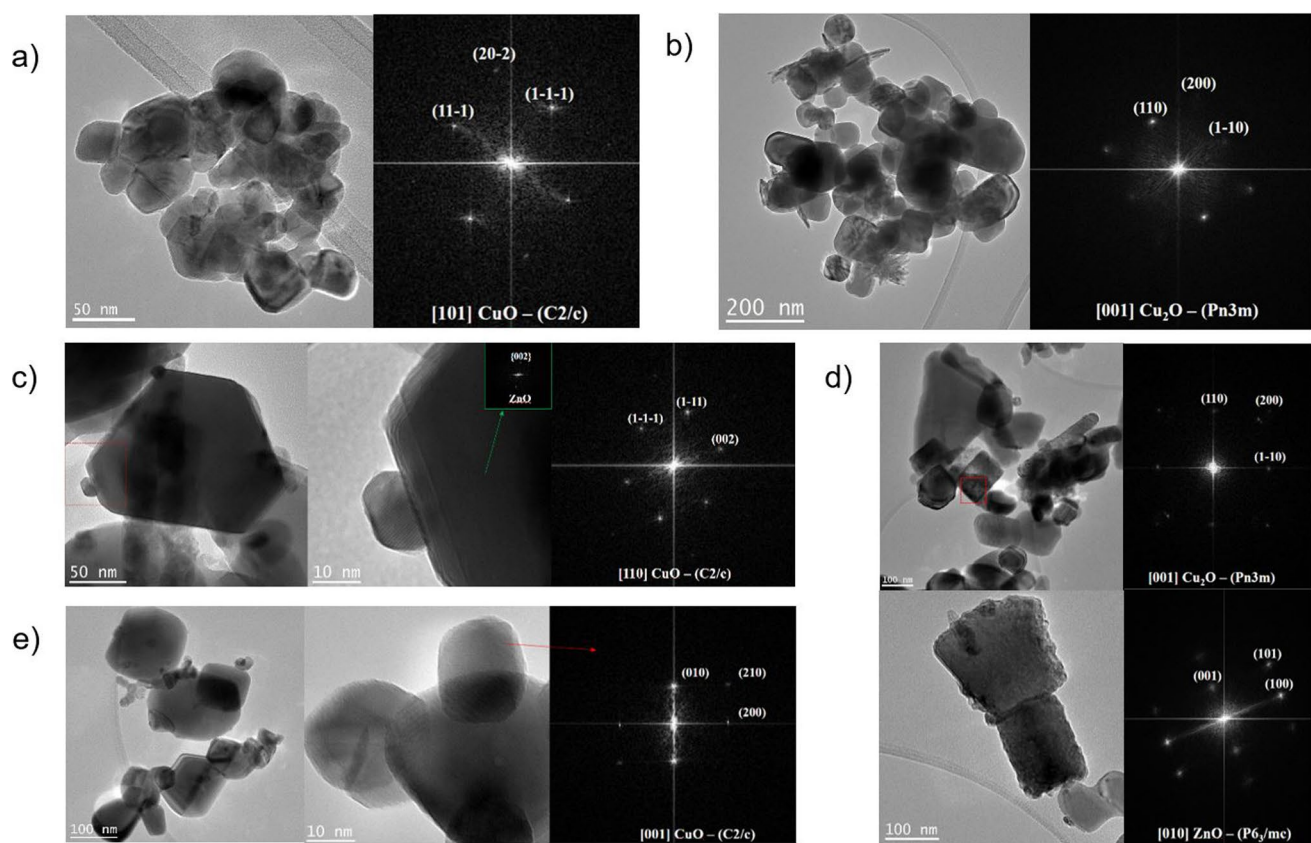


**Fig. 2** HRTEM images of synthesised catalyst and associated Fourier transforms of HRTEM images for: **a)** CuO, **b)** Cu<sub>2</sub>O, **c)** CuO/ZnO, **d)** Cu<sub>2</sub>O/ZnO, and **e)** CuO/SnO<sub>2</sub>

## Electrochemical testing

Using the RDE setup, LSVs were run for each catalyst at 500, 1000, 1500, and 2000 rpm rotation rates. As the rotation rates increase so does the produced current densities, with this effect occurring for all catalysts tested here (with all rotation rate LSV plots for all catalysts available in the supporting information, SI Fig. 9). Generally speaking, this effect occurs by enhancing the mass transfer of reactants to the working electrode through improved convection in the mass transfer process. However, given the abundant availability of water as a reactant in the aqueous electrolyte, the increased current density observed at higher rotation rates likely does not stem from improved mass transfer of the water reactant. Instead, the rotation likely helps maintain the pH at the electrode–electrolyte interface closer to the bulk pH. Monteiro et al. [30] reported that higher rotation rates during the hydrogen evolution reaction (HER) result in a smaller increase in local pH, thereby preventing the formation of a diffusion-limited plateau for hydrogen ions (H<sup>+</sup>). At the pH of the electrolyte used in this work, had the experiments been done in the absence of a buffer, we would see a diffusion-limited plateau, due to the reduction

of H<sup>+</sup>, followed by an exponentially increasing current due to the reduction of H<sub>2</sub>O. The latter would suffer no transport limitations because, as mentioned above, there is a lot of it. Because we do have a buffer, the plateau due to the diffusion-limited reduction of H<sup>+</sup> is absent (the dissociation equilibrium of the phosphate buffer provides those protons). However, despite the buffer, at high current densities, the pH at the interface will deviate from that in the bulk. Increasing rotation rates of the RDE allows to keep interfacial pH closer to bulk pH.

Figure 3a shows the LSVs for all catalysts tested here, at 2000 rpm, with the current densities reported against the corresponding catalysts electrochemically active surface areas (ECSA), in cm<sup>2</sup>, with the description of ECSA calculations described later. Along with this, all HER Tafel slopes are shown in Fig. 3b. The HER overpotentials, taken at 10 mA/cm<sup>2</sup>, are lower for the bare copper oxides compared to the supported copper oxides. Keeping in mind our ultimate goal of identifying the best supports which suppress HER to the benefit of CO<sub>2</sub>RR, higher HER overpotential values are highly desirable for the CO<sub>2</sub> reduction reaction. All catalysts evaluated here possess high overpotential values of 0.42 V vs. RHE or greater, i.e. promising results for the

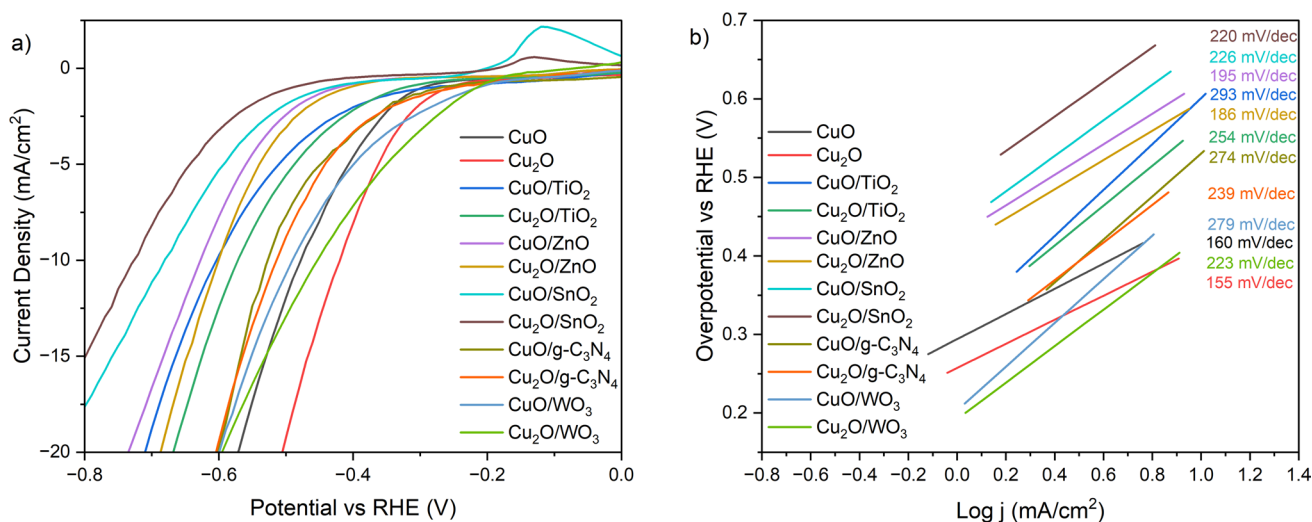


**Fig. 3** a) HER LSVs of all catalysts tested at 2000 rpm rotation rate, b) HER Tafel slopes of all tested catalysts

use of these catalysts for CO<sub>2</sub>RR. The bare copper oxides had the lowest overpotentials of 0.42 and 0.48 V vs. RHE for Cu<sub>2</sub>O and CuO respectively, and with Cu<sub>2</sub>O consistently showing lower overpotentials than CuO, when deposited onto the different supports (Table 1). Under the reducing electrochemical conditions used here, from the highly negative potentials being applied, theoretically, both the copper oxides should be reduced fully to metallic copper in situ [31, 32]. However, a difference in overpotentials is still seen for the two different oxides, therefore suggesting either; the difference in the HER catalytic activity comes from another catalyst characteristic rather than the difference in the starting oxidation state, or partial oxide phases are still present on the electrocatalysts surface. The data also shows that the addition of a support to the copper oxides can be used to further suppress the HER, with the SnO<sub>2</sub> support resulting in the largest overpotentials, along with being the only support

in which the CuO overpotential is lower compared to the Cu<sub>2</sub>O catalysts. The ZnO support results in the next best HER overpotential suppression, with values of 0.63 and 0.6 V vs. RHE for CuO and Cu<sub>2</sub>O respectively, with the TiO<sub>2</sub> support resulting in a slightly worse overpotential suppression of 0.03 V lower than ZnO, for both respective oxides. The GCN support showed to be poor at suppressing the HER overpotential, with overpotential values of 0.53 and 0.5 V vs. RHE for CuO/GCN and Cu<sub>2</sub>O/GCN respectively, significantly worse than other supports tested here. However, the WO<sub>3</sub> support was shown to be the worst at HER suppression, with CuO/WO<sub>3</sub> and Cu<sub>2</sub>O/WO<sub>3</sub> achieving overpotential values of 0.49 V and 0.45 V vs. RHE respectively, only 0.01 and 0.03 V larger than that of bare CuO and Cu<sub>2</sub>O. This increase in overpotential when depositing Cu oxides on WO<sub>3</sub> is incredibly small when compared to the 0.31 V overpotential increase achieved when depositing Cu<sub>2</sub>O onto SnO<sub>2</sub>.

**Table 1** Overpotential values (taken at 10 mA/cm<sup>2</sup>) from LSVs at 2000 rpm, Tafel slopes, double layer capacitance values (C<sub>dl</sub>), electrochemically active surface area (ECSA) values, and charge transfer resistances (from EIS at AC amplitude of 10 mV) for all catalysts tested in this work

Catalyst	Overpotential (V)	Tafel slope (mV/dec)	Exchange current density (μA/cm <sup>2</sup> )	C <sub>dl</sub> (μF)	ECSA (cm <sup>2</sup> /g)	R <sub>ct</sub> (Ω cm <sup>2</sup> )
CuO	0.48	160	14.54	60.35	1406	96.5
Cu <sub>2</sub> O	0.42	155	21.98	102.29	1449	136.9
CuO/TiO <sub>2</sub>	0.6	293	88.89	9.58	930	111.9
Cu <sub>2</sub> O/TiO <sub>2</sub>	0.57	254	59.65	11.47	1274	84.2
CuO/ZnO	0.63	195	6.54	5.54	1150	114.7
Cu <sub>2</sub> O/ZnO	0.60	186	6.25	7.56	1321	73.1
CuO/SnO <sub>2</sub>	0.69	226	11.65	45.74	784	142.0
Cu <sub>2</sub> O/SnO <sub>2</sub>	0.73	220	5.93	21.29	1192	84.5
CuO/g-C <sub>3</sub> N <sub>4</sub>	0.53	274	91.12	14.87	1023	123.4
Cu <sub>2</sub> O/g-C <sub>3</sub> N <sub>4</sub>	0.51	239	75.09	14.11	1234	66.0
CuO/WO <sub>3</sub>	0.49	279	185.7	36.92	931	68.9
Cu <sub>2</sub> O/WO <sub>3</sub>	0.45	223	137.7	63.50	1273	65.3

The HER exchange current densities for all catalysts evaluated here are available in Table 1. Supported CuO electrocatalysts achieved higher exchange current densities than supported Cu<sub>2</sub>O electrocatalysts, for all supports, with the non-supported copper oxides being the only materials to deviate from this trend. Larger exchange current densities correspond to a larger standard rate constant; therefore, the supported CuO electrocatalysts have faster standard reaction kinetics compared to supported Cu<sub>2</sub>O catalysts, for all supports. The WO<sub>3</sub> support, previously shown to be the worst at increasing the HER overpotential, also achieves the highest exchange current densities of 185.7 and 137.7  $\mu\text{A}/\text{cm}^2$ , for CuO/WO<sub>3</sub> and Cu<sub>2</sub>O/WO<sub>3</sub> respectively, significantly higher than all other catalyst tested here. This shows that the WO<sub>3</sub>-supported materials are very active HER catalysts, with the higher exchange current densities correlating to a small apparent HER activation energy, not desirable for use within the CO<sub>2</sub>RR to suppress the competing HER reaction. As seen in Table 1, ZnO and SnO<sub>2</sub> impart the lowest HER exchange current densities to Cu oxides when supported. This indicates that these supports lead to the slowest HER reaction kinetics due to their higher HER activation energies. The combination of these slow kinetics and the previously discussed high HER overpotential values demonstrate that, with ZnO or SnO<sub>2</sub> supported Cu oxides, HER is suppressed when compared to the unsupported Cu oxides. The support effect of GCN and TiO<sub>2</sub> is similar in the case of CuO oxide, with exchange current densities of 88.89  $\mu\text{A}/\text{cm}^2$  for CuO/TiO<sub>2</sub> and 91.12  $\mu\text{A}/\text{cm}^2$  for CuO/GCN, however, very different in the case of Cu<sub>2</sub>O, with the GCN support imparting an exchange current density 15.44  $\mu\text{A}/\text{cm}^2$  larger than when TiO<sub>2</sub> is used. Along with this, the GCN was also not effective at increasing the HER overpotential, making it a more HER-active material compared to TiO<sub>2</sub>. However, both GCN and TiO<sub>2</sub> supports still impart HER exchange current densities to Cu oxides significantly lower than that imparted by WO<sub>3</sub> when used to support Cu oxides. This, along with lesser HER overpotentials, makes WO<sub>3</sub> the worst choice (amongst the ones tested) of support for intrinsic HER suppression. The bare copper oxides, previously described to have the lowest HER overpotentials, exhibited the third lowest exchange current densities for each respective copper oxide, with values of 14.54 and 21.98  $\mu\text{A}/\text{cm}^2$  for CuO and Cu<sub>2</sub>O respectively. This would suggest that the bare Cu oxides have a smaller standard HER rate constant compared to their supported versions on WO<sub>3</sub>, GCN, and TiO<sub>2</sub>, showing that the use of these supports increases the standard HER rate constant.

HER Tafel slopes (Fig. 3b) are reported in Table 1. Cu<sub>2</sub>O-based electrocatalysts always have a lower Tafel slope value compared to CuO electrocatalysts, no matter the support, i.e. a trend similar to the one previously discussed in relation to the overpotential values. The Tafel

slope represents the effect the applied potential has on the reaction rate, with a lower Tafel slope showing a more pronounced decrease in the activation barrier with increased (in this case cathodic) applied potential. The unsupported Cu oxides possess the lowest Tafel slope values of 160 and 155 mV/dec for CuO and Cu<sub>2</sub>O respectively. Regardless of the previously described low HER exchange current densities for the bare oxides, these low Tafel slopes will result in a more rapid increase in the HER reaction rate as the potential is increased to more negative values. This observation, along with the fact that the unsupported Cu oxides possess the lowest HER overpotentials, suggests that the unsupported Cu oxides possess higher HER electrocatalytic activity, when compared to their supported versions, proving that, when supported, HER can be inhibited at high cathodic potentials. It was also previously noted that supported CuO attains a higher exchange current density and, therefore, faster standard HER rate, when compared to supported Cu<sub>2</sub>O. However, for all supports, the Cu<sub>2</sub>O catalysts possess lower HER Tafel slope values, therefore resulting in a greater increase in the HER rate as an increasingly higher cathodic overpotential is applied. This along with the supported Cu<sub>2</sub>O electrocatalyst always possessing lower HER overpotential values, when compared to CuO, results in the Cu<sub>2</sub>O materials being a more HER active electrocatalyst. This can be seen in the LSV plots in Fig. 3a, where the Cu<sub>2</sub>O electrocatalysts always attain higher HER current densities at each applied potential, compared to CuO for each support, with the SnO<sub>2</sub> support being the exception to this trend. The TiO<sub>2</sub>-supported electrocatalysts were shown to have the highest Tafel slope values of 293 and 254 mV/dec, for CuO/TiO<sub>2</sub> and Cu<sub>2</sub>O/TiO<sub>2</sub> respectively, suggesting that their HER rate shows the smallest changes as a more cathodic overpotential is applied (i.e. smaller decrease of the activation barrier with applied potential). The TiO<sub>2</sub> catalysts were previously discussed to possess undesirable HER intrinsic properties, with high exchange current densities and lower onset overpotentials; however, these high HER Tafel slopes are a more desirable characteristic, resulting in a more cathodic overpotential needed to be applied to increase the HER current density. Out of all the supported catalysts, the ZnO produced the lowest HER Tafel slopes, followed by the SnO<sub>2</sub>, the two supports previously discussed to show desirable properties for suppressing HER. Due to these lower Tafel slope values for the ZnO support, as a more cathodic potential is applied, eventually ZnO-supported Cu oxides will generate higher current densities than TiO<sub>2</sub>-supported Cu oxides, as seen in Fig. 3a. However, for the SnO<sub>2</sub>-supported catalysts, even with this undesirably low HER Tafel slope, the significantly higher onset overpotentials in comparison to the other supported catalysts will still result in a lower generated HER current

density across the potential window tested here, making it the best HER suppressor amongst the supports employed in this work. An opposite behaviour as the one observed for ZnO and SnO<sub>2</sub>-supported Cu oxides was observed for WO<sub>3</sub>. The WO<sub>3</sub>-supported catalysts achieved the lowest HER overpotentials for all supports assessed here, along with the highest HER exchange current densities, i.e. not ideal characteristics for suppressing HER. However, they exhibited larger HER Tafel slope values than most of the other supports, with values of 279 and 223 mV/dec, for CuO/WO<sub>3</sub> and Cu<sub>2</sub>O/WO<sub>3</sub> respectively. This implies that when anchoring Cu oxides onto WO<sub>3</sub>, the standard activation energy barrier is small in comparison to other supports, but this activation barrier sees smaller changes as the applied cathodic potential is increased, and therefore smaller increases in the HER rate. This is a desirable catalyst characteristic for suppressing HER. Despite this, the WO<sub>3</sub> support is still a poor HER suppressor due to its significantly lower overpotential, resulting in higher HER current densities being achieved at the same applied potentials compared to most other supports (Fig. 3a). The GCN support exhibited similar issues as the WO<sub>3</sub> support in terms of suppressing HER, i.e. similar Tafel slopes as WO<sub>3</sub>-supported Cu oxides, but low HER overpotentials.

The electrochemically active surface area (ECSA) is one of the main factors driving the activity of an electrocatalyst, making it a vital characteristic to evaluate for describing how a support might suppress HER. Determination of the ECSA of materials like those used in this study is a really challenging exercise in experimental electrochemistry. In this work, the ECSA is determined from the double layer capacitance ( $C_{dl}$ ) obtained from cyclic voltammograms measured in the non-faradaic potential window of 0.23 to 0.43 V vs. RHE, at scan rates 10, 20, 30, 40, and 50 mV/s. The resulting CV's can be found in the supporting information (SI Fig. 10). Figure 4 shows the linear relationship between the  $(J_{anodic} - J_{cathodic})/2$ , taken at 0.33 V vs. RHE from each CV, against the scan rate, with the gradients being equal to the  $C_{dl}$ , which numerical values are reported in Table 1. The voltammograms in the non-faradaic window, from which  $C_{dl}$  is derived, correspond to the response of the whole electrode, i.e. glassy carbon substrate + support material + Cu oxide-based electrocatalyst. Although we have not disentangled the contribution of the glassy carbon substrate of the RDE tip to the overall double layer capacitance, we work on the assumption that this contribution is almost identical for all the samples examined in this work, and therefore, the obtained  $C_{dl}$  values still provide a useful comparison between the different electrocatalysts.

The unsupported Cu oxides resulted in the largest  $C_{dl}$  values of 102.19 and 60.35  $\mu\text{F}$  for Cu<sub>2</sub>O and CuO respectively. The introduction of the supports resulted in

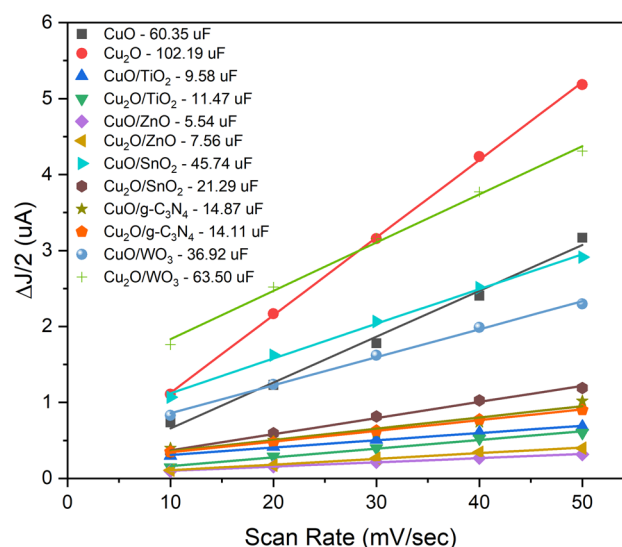


**Fig. 4** Linear relation between scan rate and  $\Delta J/2$  at 0.33 V (vs. RHE) obtained from a single CV at every scan rate

a decrease in the double layer capacitance values, with the ZnO support producing the lowest values, followed by TiO<sub>2</sub>. From double layer capacitance values, ECSA can be calculated through the equation below [33]:

$$ECSA = \text{geometric surface area} \times \frac{C_{dl}'}{C_s} \quad (1)$$

with the geometric surface area being the area of the glassy carbon disk of the RDE, which is 0.126 cm<sup>2</sup>.  $C_{dl}'$  is the double layer capacitance (in gravimetric capacitance (F/g)), and  $C_s$  is the specific capacitance (F/g). The specific capacitance can be calculated via equation:

$$C_s = \frac{Q}{m\Delta V} \quad (2)$$

where Q is the average charge during the charge–discharge process of the CV, m is the catalyst mass, and  $\Delta V$  is the potential window. From this, the equation below can be derived, where the numerator is equal to the area of the CV curves [34]:

$$C_s = \frac{\int IVdv}{(2km\Delta V)} \quad (3)$$

where I and V are the CV current and potential respectively,  $\Delta V$  is the potential window for the CV, k is the scan rate (in V/s), and m is the mass of active material (in g). In determining, the gravimetric capacitance and the specific capacitance, we are introducing the approximation of not considering the mass of the glassy carbon support of the RDE tip, hence attributing the overall  $C_{dl}$  to the Cu oxides + support material only. As a result, although still useful for comparing the different supported electrocatalysts, the absolute values of ECSA (Table 1) need to be treated with caution.

Cu<sub>2</sub>O-based electrocatalysts have been shown to have higher ECSA in comparison to CuO-based electrocatalysts, for all the supports tested, following on to the previously denoted higher HER electrocatalytic activity of the Cu<sub>2</sub>O materials compared to CuO. The CuO/SnO<sub>2</sub> electrocatalyst exhibited the smallest active surface area of 784 cm<sup>2</sup>/g, significantly lower than all other catalysts, along with Cu<sub>2</sub>O/SnO<sub>2</sub> having the smallest ECSA of all Cu<sub>2</sub>O materials of 1192 cm<sup>2</sup>/g. The previously described poor HER electrocatalytic activity of the SnO<sub>2</sub> support, through small HER exchange current density and larger overpotential values, is a promising characteristic for its use in CO<sub>2</sub>RR to suppress the competing reaction; however, this significantly lower electrochemically active surface area is not a desirable catalyst characteristic for future use within CO<sub>2</sub>RR. As reported in Table 1, the ZnO support results in the catalysts with the highest ECSA out of all the supports used here, with values of 1150 and 1321 cm<sup>2</sup>/g, for CuO/ZnO and Cu<sub>2</sub>O/ZnO respectively, the highest out of all supported materials tested here. As previously discussed, ZnO-supported Cu oxides possessed the smallest HER exchange current densities, along with the second largest HER overpotentials after SnO<sub>2</sub>, making it a very good support for HER suppression. This leads to great promise of using the ZnO support within CO<sub>2</sub>RR, via significantly suppressing the HER whilst holding numerous available active sites for the reaction to take place on, with this large overpotential value and small exchange current densities allowing for lower HER current densities produced at a wide range of applied potentials, compared to other supports, regardless of its lower Tafel slope value. The TiO<sub>2</sub>-, GCN-, and WO<sub>3</sub>-supported electrocatalysts possess similar ECSA values, for both CuO and Cu<sub>2</sub>O catalysts, as seen in Table 1.

Electrochemical impedance spectroscopy (EIS) was also employed to study the electrode kinetics of the catalysts examined in this work. Nyquist plots for all catalysts were obtained, as described by Anantharaj et al. [35], at the onset potential (potential taken at  $-2 \text{ mA/cm}^2$ ) of the previously measured HER LSV curves, with EIS kinetic studies being charge transfer controlled in low overpotential regions and mass transfer controlled at larger overpotentials [36]. All the Nyquist plots measured are available in the supporting information (SI Fig. 11). The EIS measurements were performed at various amplitude potentials of 10, 50, 100, and 200 mV, with the Nyquist plot semicircles decreasing in radius size as the sinusoidal amplitude potential increases, as the potential avails the electron transfer. EIS data was compared at the lowest amplitude potential of 10 mV. Modelling EIS data using the equivalent circuit shown in the supporting information (SI Fig. 12), charge-transfer resistance ( $R_{ct}$ ) values were derived, with all  $R_{ct}$  values reported in Table 1. Smaller charge-transfer resistance values between the electrode and electrolyte allows for faster charge-transfer

kinetics, and therefore, potentially greater HER catalytic activity. Supported Cu<sub>2</sub>O electrocatalysts exhibited charge-transfer resistance values consistently lower than supported CuO electrocatalysts, with the unsupported Cu oxides being the only materials to deviate from this trend. Amongst all the electrocatalysts tested, SnO<sub>2</sub>-supported Cu oxides produced the highest charge-transfer resistance, for each respective Cu oxide, with values of 142.0 and 84.5  $\Omega \text{ cm}^2$  for CuO/SnO<sub>2</sub> and Cu<sub>2</sub>O/SnO<sub>2</sub> respectively. Interestingly, SnO<sub>2</sub>-supported Cu oxides (together with ZnO-supported Cu oxides) showed very low exchange current densities derived from Tafel plots, which is in line with expectations. The WO<sub>3</sub>-supported Cu oxides on the contrary, shown so far to be the worst (amongst the supported Cu oxides) at suppressing HER and with the highest exchange current densities from Tafel plots, also produced the lowest HER charge transfer resistance for each oxide, with values of 68.9 and 65.3  $\Omega \text{ cm}^2$ , for CuO/WO<sub>3</sub> and Cu<sub>2</sub>O/WO<sub>3</sub> respectively, which again is in line with expectations.

## Conclusion

We showed that supporting Cu oxides on oxide supports can be used as a strategy to suppress HER activity, with the unsupported Cu oxides being the most HER active, achieving the lowest overpotential and Tafel slope values for HER. The supported Cu<sub>2</sub>O electrocatalysts exhibited lower HER overpotentials and Tafel slopes compared to the CuO-based electrocatalysts, along with possessing higher electrochemically active surface areas. This greater HER activity for supported Cu<sub>2</sub>O comes despite their systematically lower exchange current densities, when compared to supported CuO, as the lower Tafel slopes and overpotentials for supported Cu<sub>2</sub>O overcome the lower exchange current densities and allow for higher HER current densities to be generated when increasingly cathodic potentials are applied. SnO<sub>2</sub> support is shown to be the most promising support for suppressing HER activity through enabling the highest HER overpotential, small HER exchange current densities, high charge transfer resistance, with higher Tafel slope values compared to the unsupported Cu oxides. ZnO support also shows great promise for suppressing HER, with the second largest overpotential values along with the smallest HER exchange current densities. This successful HER suppression from the ZnO support is achieved whilst it also holds the highest (amongst the supported Cu<sub>2</sub>O and CuO respectively) ECSA values for electrochemical reactions to occur, and despite exhibiting lower HER Tafel slopes than other supported Cu oxides (although still higher than the unsupported Cu oxides). WO<sub>3</sub> support was shown to be the most undesired support evaluated here, due to its low HER overpotentials and significantly higher exchange current

densities, in conjunction with possessing the lowest HER charge transfer resistances for each respective oxide. Following this evidenced-based analysis of the macroscopic effect of the supports, further research combining experiments and computation is currently being undertaken to assess how the different supports are modifying the active site nature and their local environment, which are modulating HER and CO<sub>2</sub>RR electrocatalytic activities.

**Supplementary Information** The online version contains supplementary material available at <https://doi.org/10.1007/s10008-025-06313-1>.

**Open Access** This article is licensed under a Creative Commons Attribution 4.0 International License, which permits use, sharing, adaptation, distribution and reproduction in any medium or format, as long as you give appropriate credit to the original author(s) and the source, provide a link to the Creative Commons licence, and indicate if changes were made. The images or other third party material in this article are included in the article's Creative Commons licence, unless indicated otherwise in a credit line to the material. If material is not included in the article's Creative Commons licence and your intended use is not permitted by statutory regulation or exceeds the permitted use, you will need to obtain permission directly from the copyright holder. To view a copy of this licence, visit <http://creativecommons.org/licenses/by/4.0/>.

## References

- Zhang X, Guo S-X, Gandionco KA, Bond AM, Zhang J (2020) *Materials Today Advances* 7:100074
- Mandal L, Yang KR, Motapothula MR, Ren D, Lobaccaro P, Patra A, Sherburne M, Batista VS, Yeo BS, Ager JW, Martin J, Venkatesan T, *Appl ACS* (2018) *Mater Interfaces* 10:8574–8584
- An R, Chen X, Fang Q, Meng Y, Li X, Cao Y (2023) *Front Chem* 11:1141453
- H. Liang, M. Li, Z. Li, W. Xie, T. Zhang and Q. Wang (2024) *Journal of CO2 Utilization* 79: 102639.
- Tabassum H, Yang X, Zou R, Wu G (2022) *Chem Catalysis* 2:1561–1593
- Khezri B, Fisher AC, Pumera M (2017) *J Mater Chem A* 5:8230–8246
- Hori Y, Wakebe H, Tsukamoto T, Koga O (1994) *Electrochim Acta* 39:1833–1839
- Abdelnaby MM, Liu K, Hassanein K, Yin Z (2021) *ChemNano-Mat* 7:969–981
- Zhi X, Jiao Y, Zheng Y, Vasileff A, Qiao S-Z (2020) *Nano Energy* 71:104601
- Peterson AA, Nørskov JK (2012) *J Phys Chem Lett* 3:251–258
- Xu C, Zhi X, Vasileff A, Wang D, Jin B, Jiao Y, Zheng Y, Qiao S-Z (2021) *Small Structures* 2:2000058
- Goyal A, Marcandalli G, Mints VA, Koper MTM (2020) *J Am Chem Soc* 142:4154–4161
- Ooka H, Figueiredo MC, Koper MTM (2017) *Langmuir* 33:9307–9313
- Khalil M, Kadja GTM, Nugroho FAA, Sutanto LG, Jiwanti PK, Abdi FF, Hussin F, Aroua MK (2024) *Renew Sustain Energy Rev* 206:114869
- Yuan J, Zhang J-J, Yang M-P, Meng W-J, Wang H, Lu J-X (2018) *Catalysts* 8:171
- Lu Y, Cao H, Xu S, Jia C, Zheng G (2021) *RSC Adv* 11:21805–21812
- Zhang H, Sun Y, Wang J, Gao X, Tang Z, Li S, Hou Z, Wang X, Nie K, Xie J, Yang Z, Yan Y-M, *Appl ACS* (2023) *Energy Mater* 6:11448–11457
- Zhang S, Kang P, Meyer TJ (2014) *J Am Chem Soc* 136:1734–1737
- Li Q, Fu J, Zhu W, Chen Z, Shen B, Wu L, Xi Z, Wang T, Lu G, Zhu J, Sun S (2017) *J Am Chem Soc* 139:4290–4293
- Zhang S, Li M, Hua B, Duan N, Ding S, Bergens S, Shankar K, Luo J (2019) *ChemCatChem* 11:4147–4153
- Sarfraz S, Garcia-Esparza AT, Jedidi A, Cavallo L, Takanabe K (2016) *ACS Catal* 6:2842–2851
- Xu K, Zhang Q, Zhou X, Zhu M, Chen H (2023) *Nanomaterials* 13:1683
- Won DH, Shin H, Koh J, Chung J, Lee HS, Kim H, Woo SI (2016) *Angew Chem Int Ed* 55:9297–9300
- Albo J, Alvarez-Guerra M, Castaño P, Irabien A (2015) *Green Chem* 17:2304–2324
- Guzmán H, Salomone F, Bensaid S, Castellino M, Russo N, Hernández S, *Appl ACS* (2022) *Mater Interfaces* 14:517–530
- C. Azenha, C. Mateos-Pedrero, T. Lagarteira and A. M. Mendes (2023) *Journal of CO2 Utilization* 68: 102368.
- Jiao Y, Zheng Y, Chen P, Jaroniec M, Qiao S-Z (2017) *J Am Chem Soc* 139:18093–18100
- Yan Z, Wu T (2022) *IJMS* 23:14381
- Rutkowska IA, Chmielnicka A, Krzywiecki M, Kulesza PJ, Meas ACS (2022) *Sci Au* 2:553–567
- Monteiro MCO, Liu X, Hagedoorn BJJ, Snabilié DD, Koper MTM (2022) *ChemElectroChem* 9:e202101223
- Delmo EP, Wang Y, Song Y, Zhu S, Zhang H, Xu H, Li T, Jang J, Kwon Y, Wang Y, Shao M (2024) *J Am Chem Soc* 146:1935–1945
- Chen C, Yan X, Wu Y, Liu S, Sun X, Zhu Q, Feng R, Wu T, Qian Q, Liu H, Zheng L, Zhang J, Han B (2021) *Chem Sci* 12:5938–5943
- Karmakar A, Kundu S (2023) *Materials Today Energy* 33:101259
- Sharma S, Chand P (2023) *Results in Chemistry* 5:100885
- S. Anantharaj, S. R. Ede, K. Karthick, S. Sam Sankar, K. Sangeetha, P. E. Karthik and S. Kundu (2018) *Energy Environ Sci* 11:744–771.
- Li D, Wu J, Liu T, Liu J, Yan Z, Zhen L, Feng Y (2019) *Chem Eng J* 375:122024

**Publisher's Note** Springer Nature remains neutral with regard to jurisdictional claims in published maps and institutional affiliations.